10

Photorefractive Waveguides

Detlef Kip[1] and Monika Wesner[2]

[1] Institute of Physics and Physical Technologies, Clausthal University of Technology, 38678 Clausthal-Zellerfeld, Germany, detlef.kip@tu-clausthal.de

[2] Physics Department, University of Osnabrück, 49069 Osnabrück, Germany, monika.wesner@uos.de

10.1 Introduction

In photorefractive crystals, the materials' refractive index can be altered by light illumination with spatially inhomogeneous intensity. This allows for a wide spectrum of applications, e.g., optical data storage, pattern recognition, adaptive optics, or dynamic holography [1, 2]. In this chapter, we will focus on a special geometry of photorefractive materials: Optical waveguides. On the one hand, due the high light intensities that are inherent in waveguide geometries, photorefractive effects in optical waveguides [3, 4] are feared as optical damage, as they can degrade the performance of integrated optical devices. On the other hand, both dynamic wave mixing and permanent holographic gratings in waveguides are of considerable interest for the development of new components for integrated optics.

In this contribution, we will focus on photorefractive waveguides in oxide crystals, and have to redirect the interested reader to other chapters of this book for materials like semiconductors or photorefractive polymers. After some basics on optical waveguide properties, a review of recent results and techniques for waveguide formation is given. Here investigations in materials with illmenite structure ($LiNbO_3$, $LiTaO_3$), perovscites ($BaTiO_3$, $KNbO_3$), crystals with tungsten-bronze structure (SBN, KNSBN), and sillenites (BSO, BTO, BGO) are discussed. As an outlook, the suitability of photorefractive waveguides for applications is demonstrated in some examples.

10.2 Fundamentals of Photorefractive Waveguides

In this section, we will briefly discuss the fundamentals of photorefractive optical waveguides as well as the experimental techniques for, e.g., the determination of refractive index profiles, electrooptic properties, and light-induced refractive index changes in waveguide samples.

10.2.1 Optical Waveguides

Optical waveguides are the key components for the development of integrated optical devices. In integrated optics, several optical components, like lasers, beam splitters, or modulators, are integrated on a suitable substrate material [5]. Here optical waveguides provide the connections between these components.

An optical waveguide consists of a dielectric material that is surrounded by another dielectric material of lower refractive index. Guidance of light is based on total internal reflection of electromagnetic waves at the boundaries of the inner medium so that radiation into the surrounding medium is forbidden. One can distinguish between planar waveguides, where the light is confined along one transverse direction while diffracting along the other transverse coordinate, and two-dimensional waveguides, where the light is guided in both transverse directions (Fig. 10.1). In the latter case, typical geometries are either channel or strip waveguides, respectively, and optical fibers with radial symmetry.

To discuss some fundamental properties of dielectric waveguides, we consider a planar structure as in Fig. 10.1a. In a ray-optics picture of waveguiding, light is guided by multiple reflections from two parallel infinite plane boundaries that act as lossless mirrors. For an electromagnetic analysis of this structure, each ray is described by a plane wave, where the total electromagnetic field consists of the sum of these plane waves. Here the self-consistency condition requires that, as a wave is reflected twice at the upper and lower boundary, its phase has to undergo a phase shift of multiples of 2π, i.e., the wave has to reproduce itself. In this way, discrete solutions for the electromagnetic field are obtained that are called the modes of the waveguide. These modes have a certain transverse electromagnetic field that is maintained during propagation along the waveguide. Depending on the light polarization, one can distinguish between TE (transverse electric) modes, where the transverse electric field points perpendicular to the waveguide normal and the propagation direction, and TM (transverse magnetic) waves, where the magnetic field is along this direction. Each mode is fully described by its transverse mode profile, its polarization, and the propagation constant $\beta = k_0 n_{\text{eff}}$, where k_0 is the wave number and n_{eff} is the effective refractive index of the mode.
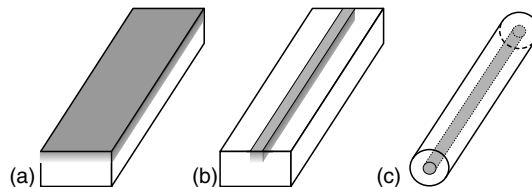

FIGURE. 10.1. Different types of optical waveguides. a) Planar waveguide; b) channel waveguide, and c) optical fiber.

The most simple case of a planar waveguide is that with a step-like refractive index jump at the boundary ($x = d$) of substrate and waveguiding layer, and another jump at the boundary of the waveguide and the top cladding ($x = 0$), which is usually air (see left part of Fig. 10.2a). In analogy to the eigenfunctions of a step-like potential well, the waveguide modes are harmonic functions, where the field amplitude exponentially decays in the cladding and substrate layers, respectively. For these modes, the effective refractive index n_{eff} is larger then the two indices of the surrounding layers. If n_{eff} is close to but slightly lower than the index of the substrate material, leaky or substrate modes of the waveguide can be excited that continuously loose energy to the substrate.

A more general profile is that of a graded-index waveguide, where the refractive index of the waveguiding layer continuously decreases from a higher surface value to the substrate refractive index. Typical examples for this type are in-diffused waveguides where the refractive index profile is determined by the diffusion profile of some in-diffused species. As a main difference to step-like profiles, different modes of a graded-index waveguide propagate in different effective depths d_{eff} of the waveguiding layer. Examples of the electric field distribution E_m of the first modes $m = 0$, 1, and 2 of a step-like and a graded-index waveguide are given in Fig. 10.2.

A universal method for coupling light into and out of a planar waveguide is the use of prism coupler. Prism coupler allow a direct measurement of the coupling efficiency as well as a mode selective excitation of the waveguide, which may be preferred for the investigation of multimode waveguides where depth dependent measurements of waveguide properties become possible in this way. Grating couplers may be used as well, but fabrication is difficult and coupling efficiencies are often low. Direct endface coupling is of particular interest for waveguides in BaTiO$_3$, KNbO$_3$, or SBN, because sample dimensions are usually small, and mechanical stress that is inherent in the prism-waveguide coupler may not be applied to these materials.
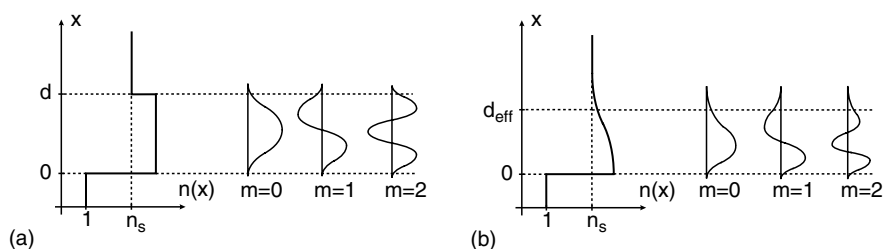

FIGURE. 10.2. Typical refractive index profiles and electric field distribution E_m of the lowest guided modes for a) step-like and b) graded-index planar waveguide.

292   Detlef Kip and Monika Wesner

10.2.2 Photorefractive Effects in Waveguide Samples

Photorefractive effects in planar waveguides can be studied by two principal holographic methods: A two-beam interferometric setup, or by monitoring the output intensity and the beam shape of a single guided beam. Here, similar as for bulk samples, a wide range of different holographic measurement techniques exists, which allow for the determination of photorefractive parameters like saturated refractive index changes, dark and photoconductivity, photovoltaic constants, or holographic sensitivity. For the investigation of channel waveguides often pump-probe techniques are utilized, where a low-power beam of larger wavelength is used to probe the refractive index change that are induced by a stronger pump beam.

   An overview of different geometries for recording of elementary refractive index gratings in waveguide samples is given in Fig. 10.3. In a standard setup gratings are written by two guided beams of the same polarization and mode number intersecting inside the waveguide (Fig. 10.3a and 10.3b). For light coupling into and out of the sample, either prism couplers or direct endface coupling can be used. Alternatively, the two beams may differ in polarization or mode number. Furthermore, gratings may be written in planar (Fig. 10.3c) or channel waveguides (Fig. 10.3d) by external beams that impinge upon the surface of the waveguiding layer. To record grating coupler for in- and out-coupling of light from the waveguide the interaction of substrate and guided modes can be used, too (Fig. 10.3e).
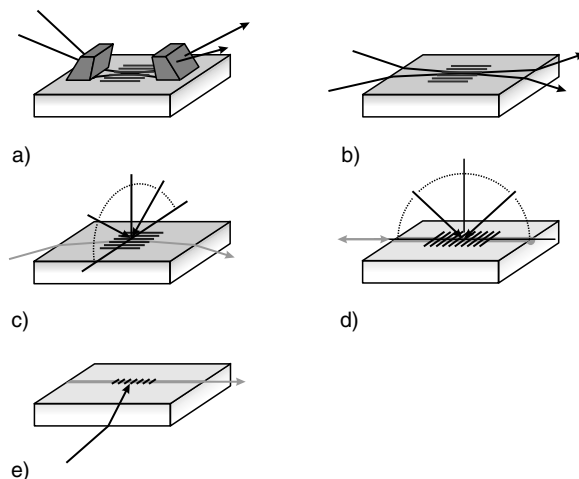

FIGURE. 10.3. Geometries for recording of holographic gratings in waveguides using either guided waves or external writing beams. a) Two-beam interference of guided beams using prism couplers or b) endface coupling, c) grating recording with external beams, d) reflection holograms in channel waveguides, and e) recording of grating couplers.

The light-induced charge transport in photorefractive oxide crystals is treated in detail in other chapters of this book. In general, the obtained models and equations for one and more photorefractive centers and for different mechanisms of charge redistribution can be transferred to waveguide samples, too. However, in most investigations of photorefractive waveguides, averaged quantities have been used to describe both, the light distribution inside the sample and the photorefractive properties. Examples are effective widths and propagation depths of the excited modes, averaged light intensities, or refractive index changes and photovoltaic constants where the values are averaged over the depth of the waveguiding layer [6]. For these averaged quantities, the Kogelnik theory of the interaction of plane waves can be used to interpret the results. As an example, the averaged refractive index change of mode m of a y-cut planar waveguide is described by

$$(<\Delta n>)_m = \frac{\int |E_m(y)|^2 \Delta n(y)\, dy}{\int |E_m(y)|^2 dy},$$

(10.1)

where the diffraction efficiency η of a grating of length d that is read out with a wavelength λ is described by a modified Kogelnik equation

$$\eta = \sin^2 \left(\frac{\pi(<\Delta n>)_m d}{\lambda} \right).$$

(10.2)

However, in some cases, the simplified treatment of the interacting beams as plane waves has failed to describe the experimental observations. In this case, the exact two-dimensional intensity distribution has to be taken into account. For example, the two-wave interaction of Gaussian beams in a multimode planar waveguiding layer can be interpreted in terms of a two-dimensionally varying time constant for the grating build-up time. This time constant is smallest in the beam center and shows an additional variation with depth [7], thus the resulting time dependence of the wave mixing, i.e., the build-up of a refractive index grating, may show significant deviations from a mono-exponential behavior.

When only a single beam is coupled into a planar photorefractive waveguide, both, light-induced phase changes in the beam path and holographic scattering reduce the transmitted power in the beam direction [8, 9]. In this case photoconductivity, refractive index changes, and holographic sensitivity can be quantitatively determined by variation of the input power and time dependent measurements of the resulting changes in the shape of the outcoupled intensity spectrum [10].

10.2.3 Experimental Methods

Different methods can be used for the fabrication of waveguides in photorefractive crystals. Typical examples are diffusion, ion exchange, implantation of ions, or the deposition of thin epitaxial layers. As the different techniques are

predominantly specific for one class of oxide crystals, a detailed description of the waveguide fabrication method is given in the respective material subsections of the next section. Here we will give a short overview on different techniques for the reconstruction of refractive index profiles and the measurement of electro-optic coefficients, as well as on the holographic investigation methods that can be used for the determination of photorefractive properties.

Refractive index profiles with typical dimensions of only a few micrometers can hardly be determined by direct measurement. Very often the reconstruction of planar waveguide profiles is based on a set of measured effective refractive indices $n_{\text{eff},i}$, which can be determined by dark-line or mode spectroscopy [11]. Here two different strategies have been established. At first, one may assume a family of plausible profiles that are characterized by a set of fit parameters. With this method, good results have been obtained for ion-implanted waveguides [12, 13], where the profiles can be well predicted by using simulations of the implantation process. A second procedure commonly used for profile reconstruction of multimode waveguides is the inverse WKB method [14]. For channel waveguides, different numerical approximations are used to calculate the effective refractive indices of the modes of an assumed or given refractive index profile, e.g., the methods of finite differences or finite elements.

Although the electro-optic properties of substrate materials for waveguide fabrication are well known in most cases, these values may differ for waveguides because of material changes that are due to the waveguide fabrication itself. Therefore techniques have been developed to measure electro-optic coefficients in both planar and channel waveguides. In planar waveguides, attenuated total reflection (ATR) spectroscopy may be used, a method that is well known from the investigation of electro-optic polymer layers [15, 16]. Alternatively, interferometric methods can be applied [17, 18]. In channel waveguides, the electro-optically induced phase changes in integrated Mach-Zehnder [19] or Fabry-Perot interferometers [20] have been used to measure electro-optic coefficients in $LiNbO_3$ and $LiTaO_3$ samples.

10.3 Materials with Illmenite Structure

Among all ferroelectric materials, photorefractive effects have been studied most extensively in lithium niobate ($LiNbO_3$) [1]. Crystals with diameters up to six inches and of superior optical quality can be grown, which makes this material the preferred candidate for applications in integrated optics. $LiNbO_3$ has large electro-optic and SHG coefficients of $r_{33} \approx 30\,\text{pm/V}$ and $d_{33} \approx 32\,\text{pm/V}$, respectively. Typical devices realized in $LiNbO_3$ waveguides are integrated lasers [21], electrooptic modulators with low half-wave voltages, quasi-phase matched structures for frequency conversion, or integrated Sagnac interferometers for high-precision rotation sensing.

Lithium tantalate ($LiTaO_3$) possesses electro-optic, nonlinear optical, and photorefractive properties similar to $LiNbO_3$. On the one hand, in some aspects

$LiTaO_3$ is even more attractive for applications in integrated optics than $LiNbO_3$. It is less sensitive to optical damage, it has a larger transparency in the UV down to 270 nm, and it has a smaller birefringence. However, high temperature waveguide fabrication that exceeds the Curie temperature of about $620°C$ (for the congruently melting composition) requires additional repoling, and crystal growth is more difficult because of the high melting point of $LiTaO_3$ of about $1650°C$. Nevertheless, waveguide devices for electro-optic modulation and frequency doubling in the visible spectral region are now commercially available.

Advantages of $LiNbO_3$ and also $LiTaO_3$ are the possibility to form low-loss waveguides, the chemical and mechanical resistance, a wide range of nonlinear optical interactions, and finally the availability of large crystals at a reasonable cost. Because of the relatively empty illmenite lattice structure, many metal ions can be indiffused into $LiNbO_3$ and $LiTaO_3$ to form low-loss waveguiding layers or channels. Titanium diffusion into $LiNbO_3$ is by far the most common technique for waveguide fabrication. On the other hand, diffusion is also an easy method to increase the photorefractive sensitivity by surface doping of the waveguide substrates. As an alternative method for waveguide formation the proton exchange technique in $LiNbO_3$ and $LiTaO_3$ has proved to result in low-loss waveguides, which are particularly well suited for applications where high intensities occur, e.g., for second harmonic generation of blue and green light.

Besides the two methods mentioned above a wide range of different epitaxial techniques has been developed in the past. A large number of oxide crystals have been fabricated in thin film form by, e.g., sputtering of a suitable target material, including the materials $LiNbO_3$ and $LiTaO_3$. These techniques include diode, reactive, ion beam, magnetron, bias sputtering, or pulsed laser deposition (PLD), as well as liquid phase epitaxy (LPE) [22] and molecular beam epitaxy (MBE) [23]. Here PLD and MBE allows fabrication of films with high optical quality and nonlinear properties that are similar to the bulk material [24, 25].

10.3.1 Titanium Diffusion

The diffusion of thin films of titanium evaporated or sputtered onto the substrate surface is a widely used method for waveguide formation in $LiNbO_3$ and in part also in $LiTaO_3$ crystals, and most of the integrated optical devices available today are based on titanium-diffused $LiNbO_3$ waveguides. In $LiNbO_3$ the extraordinary refractive index increases linearly with titanium concentration, whereas the ordinary index shows a slightly sublinear behavior [26]. Larger changes are obtained for extraordinarily polarized light. No significant reduction of the electro-optic or nonlinear optical coefficients have been reported. Diffusion of titanium has been used to produce waveguides in $LiTaO_3$ [27], too. The low diffusion coefficient requires temperatures of above $1300°C$, thus exceeding the material's Curie temperature, which requires additional poling of the samples.

The diffusion process has been investigated in detail in $LiNbO_3$ and consists of several complex steps [28, 29]. Here annealing is usually performed at temperatures around $1000°C$. At about $500°C$, titanium is oxidized to TiO_2, and above $600°C$ $LiNb_3O_8$ epitaxial crystallites are formed at the surface, connected with a loss of lithium. For temperatures larger than $950°C$, a $(Ti_{0.65}Nb_{0.35})O_2$ mixed oxide appears, which acts as the diffusion source for titanium indiffusion. With increasing annealing time, titanium diffuses deeper into the crystal, and the titanium-niobium oxide layer decomposes. For temperatures above $600°C$, a loss of Li or Li_2O at the crystal surface is observed. Because this mechanism increases the extraordinary refractive index Li, out-diffusion has to be prevented in particular for channel waveguide formation. This is often realized by annealing of the samples in water vapor or a Li-rich atmosphere.

Besides titanium a large number of other metals can be diffused into $LiNbO_3$ to form waveguiding layers, e.g., iron, copper, vanadium, nickel, niobium, cobalt, silver, or gold [30]. Here zinc is of special interest as the diffusion of zinc into $LiNbO_3$ has been found to produce low-loss waveguides with higher resistance to optical damage [31, 32] when compared to titanium.

Planar and channel $LiTaO_3$ waveguides have been fabricated by diffusion of, e.g., titanium [27], niobium [33], or zinc [20]. For this high-temperature process, repoling of the samples is necessary to recover the electro-optic properties of $LiTaO_3$.

For application of the photorefractive effect, waveguides fabricated by combined titanium and iron or copper diffusion, respectively, have shown considerably improved holographic sensitivity [34, 35].

10.3.2 Proton Exchange

Proton exchange (PE) is a low temperature process ($T < 250°C$) that has been successfully used for waveguide fabrication in $LiNbO_3$ [36, 37] and $LiTaO_3$ [38, 39]. Basically, hydrogen that is provided by an appropriate acid is partially exchanged for lithium ions of the crystal. In the case of $LiNbO_3$, the chemical composition $Li_{1-x}H_xNbO_3$ is formed where x, $0 \le x \le 1$, is the exchange degree.

A widely used technique for the formation of proton-exchanged waveguides is the immersion of the substrate in a bath of molten benzoic acid [37]. This liquid-phase treatment produces a mixture of crystalline β-phases on the sample surface with an exchange degree in the range of $0.5 < x < 0.85$ [40], and a nearly step-like refractive index profile. The maximum index change depends on the used acid. Typical values for benzoic acid are $\delta n_e = 0.12$, $\delta n_o = -0.05$ ($LiNbO_3$, [36]) and $\delta n_e = 0.02$, $\delta n_o \approx 0$ ($LiTaO_3$, [39, 41]), and higher changes up to $\delta n_e = 0.145$ [42] for $LiNbO_3$ are obtained using phosphoric acid. When using benzoic acid, the acidity of the melt can be diluted by the addition of some mol percent of lithium benzoate [36]. In this way, $LiNbO_3$ channel waveguides fabricated with pure benzoic acid show typical propagation losses

between 0.5 and $1 \, \text{cm}^{-1}$ for extraordinarily polarized light, while lower values of about $0.2 \, \text{cm}^{-1}$ have been reported for the use of phosphoric acid [42].

A significant degradation of electro-optic and nonlinear optical properties of proton-exchanged $LiNbO_3$ waveguides was found very early [43], which is caused by the lattice disorder and mixture of β-phases in strongly exchanged layers [44, 45]. A partial solution to this problem is the use of an additional post-annealing treatment at temperatures above $350^\circ C$ [19]. These so-called annealed proton-exchanged (APE) waveguides have a graded refractive index profile. The waveguiding layer is completely converted to the α-phase [44] with $x < 0.12$ and an index change of $\delta n_e < 0.03$ [16]. Furthermore, for APE waveguides, very small loss coefficients of about $0.03 \, \text{cm}^{-1}$ have been measured [46]. Alternatively, waveguides with well defined phases can be obtained by carefully controlling the exchange degree. In this case, large electrooptic coefficients for PE layers up to $r_{33} = 22 \, \text{pm/V}$ for $LiNbO_3$ can be obtained without additional annealing treatment [47]. In most work on proton-exchanged $LiTaO_3$ waveguides, electro-optic coefficients have been found to be strongly decreased after the exchange [48], and the values were at least partially restored after additional annealing treatment [17, 18, 410].

Very recently a new method, vapor-phase proton exchange (VPE) has been reported for $LiNbO_3$ [50] and $LiTaO_3$ [51], which results in high damage resistance, low optical losses ($\alpha < 0.1 \, \text{cm}^{-1}$), and fully preserved electro-optic and nonlinear properties. For this method, samples are treated in an evacuated ampoule with benzoic acid powder at the bottom while the substrate is held in the top of the ampoule. Typical annealing temperatures are about $300^\circ C$ and exchange times vary from several hours to a few days. As for the PE process, the resulting VPE waveguides have a nearly step-like index profile, and for not-too-long exchange times, a high-quality κ_2 phase structure can be obtained that is well suited for nonlinear optical applications [52].

By using proton exchange in $LiNbO_3$ and $LiTaO_3$, waveguides with strongly enhanced photorefractive sensitivity can be fabricated when the exchange of protons is combined with a successive copper exchange from melts containing Cu^+ or Cu^{2+} ions [16, 53]. As this technique of copper doping is a low-temperature process well below the Curie temperature of, e.g., $LiTaO_3$, it is of particular interest for the fabrication of photorefractive waveguides in this material.

10.3.3 Lithium Niobate Waveguides

Light-induced refractive index changes in optical materials can be considered from two points of view. On the one hand, these photorefractive effects are of considerable interest for applications in information storage and optical communication technology. On the other hand, the same mechanism is feared as optical damage; e.g., in waveguide devices, light-induced phase shifts may degrade the optical performance. The latter is particularly important for nonlinear applications of $LiNbO_3$ waveguides, where the performance of integrated

modulators and switches, lasers, or optical parametric oscillators may suffer from optical damage effects.

Optical Damage in Planar Waveguides

The optical damage resistance of planar $LiNbO_3$ waveguides fabricated by proton exchange, annealed proton exchange, vapor-phase proton exchange, metal diffusion, and epitaxy has been investigated in many works. However, a detailed comparison of the different methods still remains difficult. Although most of the used substrates are nominally undoped, they may differ a lot in the remaining impurity concentration. What is even more difficult is the influence of different light intensities and wavelengths when probing optical damage. In general, steady-state refractive index changes, holographic sensitivity, and photoconductivity depend on light intensity [54, 55]. For certain fabrication methods, both dark and photoconductivity of the waveguiding layer are considerably enlarged, and particularly at higher light intensities more than one photorefractive center can be involved in the charge transport [56], thus making the above quantities intensity dependent. Therefore, we restrict ourselves to some general remarks regarding photorefractive effects in differently prepared waveguides. A qualitative overview of some properties of $LiNbO_3$ waveguides is given in Table 10.1. For a more detailed comparison of photorefractive $LiNbO_3$ waveguide properties, see Ref. [4].

For titanium-diffused waveguides, high holographic sensitivity and large light-induced refractive index changes have been found [10]. It has been recognized that Fe^{2+} centers are stabilized by Ti^{4+} ions against oxidation [6], thus increasing the sensitivity to optical damage. On the other hand, a higher photorefractive damage resistance has been obtained for waveguides prepared by the diffusion of zinc into $LiNbO_3$ and for moderate light intensities of the order of $10^5 W/cm^2$ [31]. This may be attributed to a reduction of anti-site defects, where zinc ions are build-in on empty lithium sites instead of niobium.

Proton exchange leads to lower values of holographic sensitivity both for annealed (APE), non-annealed (PE), and vapor-phase (VPE) treated samples

TABLE. 10.1. Overview of general photorefractive properties (optical damage or saturated refractive index change, photoconductivity, holographic sensitivity, and temporal stability of refractive index profiles) of $LiNbO_3$ waveguides fabricated by different methods: PE, proton exchange; APE, annealed proton exchange; VPE, vapor-phase proton exchange. These properties are only a general tendency of the different processes.

Fabrication	Opt. damage	Photoconduct.	Hol. sensitivity	Temporal stab.
Ti-Diffusion	High	Low	High	High
PE	Moderate	High	Low	Low
APE	Moderate	Moderate	Moderate	Moderate
VPE	Moderate/Low	Moderate	Low	Moderate/High

[10, 50, 57] when compared with titanium diffusion. In strongly exchanged waveguides, no light-induced refractive index changes are found [58], and this effect has been attributed to both a large increase of dark and photoconductivity [54], and a strong degradation of the electro-optic properties [43]. Here a conversion of Fe^{2+} to Fe^{3+} has been found for the proton exchange process [59], which can explain the observed decrease in holographic sensitivity, too.

In thermal fixing of holographic gratings in $LiNbO_3$ and $LiTaO_3$ at elevated temperatures, protons are believed to compensate for the electronic space charge field [55, 60]. In proton-exchanged waveguides, a similar mechanism is observed at room temperature, when light-induced electronic charge gratings are compensated for by light-insensitive, positively charged ions [61, 62], which may be explained by a considerably enlarged protonic conductivity of the PE layers.

Annealing treatment of PE layers with a higher exchange ratio leads to a recovery of the electro-optic coefficients [19, 47], while at the same time photoconductivity only slightly decreases [54]. Although the holographic sensitivity of APE samples is thus increased with annealing time, it is still two orders of magnitude lower than for titanium in-diffused samples. Excellent results have been obtained for vapor-phase proton-exchanged layers, where the photorefractive damage threshold has been reduced by one to two orders of magnitude when compared to APE samples [50]. On the other hand, the use of MgO-doped $LiNbO_3$ substrates for proton exchange has resulted in only slightly enlarged photorefractive damage resistance [57].

Planar waveguides fabricated by LPE [22] have shown higher holographic sensitivity than PE samples, but the values are still lower than for titanium diffusion [10, 24]. Other methods of thin film deposition have recently been used to grow epitaxial $LiNbO_3$ layers, e.g., sputtering [63], the sol-gel process [64], and PLD [25], but no photorefractive properties have been reported.

Wave-Mixing and Scattering

Quite a few optical wave mixing experiments have been performed in planar $LiNbO_3$ waveguides, and most of the used samples were treated to enhance photorefractive effects, e.g., by iron or copper in-diffusion, or combined proton and copper exchange. The published work may be subdivided into isotropic wave mixing, where the interacting light beams have the same polarization, and anisotropic wave mixing, where orthogonally polarized modes interact.

In contrast to wave mixing in the bulk where elementary refractive index gratings are usually recorded utilizing plane waves, in waveguides the inhomogeneity of the interacting fields and the presence of different modes have to be taken into account [34, 65, 66]. As a result, several photorefractive processes have been identified in waveguides that have no true analogs in volume crystals, e.g., polarization conversion of copropagating TE and TM modes [67, 68], or the recording of gratings where the photovoltaic current flows perpendicular to the grating vector [69].

In multimode planar waveguides, light can be scattered under discrete angles from an excited mode into other modes with different mode indices, but with the same polarization. In this interaction, the pump and the scattered waves have to fulfill a corresponding phase matching condition, thus stray light can be amplified by parametric interaction. Because light waves that belong to different modes of the waveguide are involved in this type of wave mixing, the interaction is called parametric inter-mode scattering [34, 70, 71].

In LiNbO$_3$ as well as in LiTaO$_3$ waveguides, orthogonally polarized modes can write holographic gratings via photovoltaic currents, enabling strong anisotropic wave mixing [67] and the generation of phase-conjugate [72] waves. This interaction, also known as polarization conversion, was observed first in y- and z-cut channel waveguides [73] and later also in planar y-cut waveguides [72, 74, 75]. The interaction can be understood by redistribution of photoexcited charge carriers by the photovoltaic effect, where the generated space-charge field is proportional to the polarization dependent photovoltaic current density [76]

$$j_k = \sum_{l,m} (\beta_{klm}^s + i\beta_{klm}^a) E_l^* E_m. \tag{10.3}$$

Here $\beta^{s,a}$ are the real linear and circular components of the photovoltaic tensor, and $E_{l,m}$ are the interacting light fields. Anisotropic interaction in LiNbO$_3$ and LiTaO$_3$ is enabled through the nondiagonal elements $\beta_{15} = \beta_{24}$ of the photovoltaic tensor. The corresponding current is modulated with the grating period $\Lambda = \lambda/(n_o - n_e)$, where λ is the light wavelength in vacuum (see Fig. 10.4).

The perturbation $\Delta\epsilon$ of the dielectric tensor has a local contribution according to β^s and a nonlocal part according to β^a [77]. As is well known, the shifted (nonlocal) grating leads to an energy exchange between the two interacting beams, where the direction of energy exchange depends on the sign of β^a. For iron-doped LiNbO$_3$, ordinarily polarized light is converted to extraordinary polarization, and for LiTaO$_3$:Fe, an opposite coupling direction is observed.
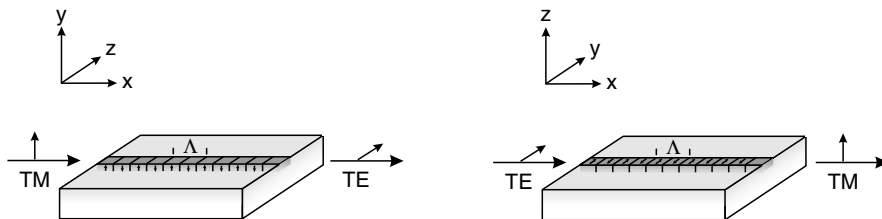

FIGURE. 10.4. Illustration of the photovoltaic current responsible for polarization conversion in LiNbO$_3$ and LiTaO$_3$ channel waveguides. a) y-cut substrate, and b) z-cut substrate. Here the c-axis is parallel to the z-axis of the sample.

Optical Damage in Channel Waveguides

Different kinds of channel waveguides in nominally pure and MgO-doped $LiNbO_3$ have been formed by titanium indiffusion, PE, APE, VPE, and ion implantation, and the corresponding photorefractive properties and damage thresholds of these waveguides have been investigated. Fujiwara et al. have compared the photorefractive properties of titanium-diffused, PE, and APE samples using an integrated Mach-Zehnder interferometer [78, 79]. For low intensities of some W/cm^2, saturated refractive index changes of titanium-diffused samples are about three orders of magnitude larger than in PE, and two orders of magnitude larger than in APE waveguides. This may be attributed to the large increase of conductivity for the PE and APE samples [79], and partly reduced electro-optic coefficients of the PE waveguides. Furthermore, holographic sensitivity is increased by a factor of four for APE waveguides [78] when compared with PE waveguides, mainly because of the restored electro-optic properties, and probably because of a further enlarged conductivity in the APE samples, too.

The use of $LiNbO_3$ doped with MgO has reduced the refractive index changes in APE channel waveguides by nearly two orders of magnitude at intensities of some kW/cm^2 [80], and photoconductivity has been decreased at the same time, too. Here it has been concluded that strongly reduced photo-voltaic currents in $LiNbO_3$: MgO waveguides are responsible for this effect.

Implantation of H^+ into $LiNbO_3$ with subsequent annealing treatment has resulted in waveguides with strong light-induced refractive index changes [81] that are larger than for APE waveguides and almost comparable with titanium-diffused samples. Simultaneously, both dark and photoconductivity are at least as high as for APE waveguides. On the other hand, strongly reduced optical damage has been found for a combination of proton exchange and ion implantation, when APE waveguides are additionally implanted with $1\,MeV\,H^+$ through the existing waveguide channels [82].

In a more recent work, light-induced shifts in the phase matching curve of second harmonic generation in both single domain and domain-inverted $LiNbO_3$ channel waveguides have been investigated by using a pump-probe technique [83]. A high photorefractive sensitivity connected with a two-step two-photon excitation has been found for single-domain samples, whereas optical damage was strongly reduced for domain-inverted samples.

10.3.4 Lithium Tantalate Waveguides

A general problem of $LiTaO_3$ waveguides is believed to be the observed instability of optical damage or light-induced refractive index changes in waveguides fabricated by diffusion or proton-exchange [84, 85]. A possible explanation for this effect might be the obtained mixture of different phases in proton-exchanged layers and a migration of protons at room temperature as well as the high number of defect sites (tantalum on lithium site) and high strain values that are inherent to crystals with non-stoichiometric composition.

Optical damage effects in zinc-diffused LiTaO$_3$ channel waveguides have been investigated in [86], and refractive index changes of $\Delta n_e \approx 5 \cdot 10^{-5}$ at a wavelength of 488 nm and an intensity of $1\,\mathrm{kW/cm^2}$ have been measured. Proton-exchanged planar LiTaO$_3$ waveguides have shown similar refractive index changes of about $4 \cdot 10^{-5}$ [87], but at a larger wavelength of 632.8 nm.

Anisotropic two- and four-wave mixing has been used to determine the photorefractive properties of titanium-diffused LiTaO$_3$:Ti:Fe waveguides [88]. In a more recent work [53], photorefractive LiTaO$_3$ waveguides were fabricated by combined proton and copper exchange at low temperatures, which avoids repoling of the samples. Here a post-annealing treatment resulted in a full recovery of the preferred α-phase of LiTaO$_3$ [53, 89].

Thin epitaxial LiTaO$_3$ films have been grown by different methods, and research has been stimulated again recently by the large interest in LiTaO$_3$ waveguides with domain-inverted structures for second harmonic generation. An overview of recent work can be found in [90].

10.4 Materials with Perovscite Structure

10.4.1 Ion Implantation

Because of the low-temperature phase transitions, large chemical inertness, and the densely packed perovscite lattice, waveguide formation techniques like ion diffusion or exchange are more difficult in crystals with perovscite structure like BaTiO$_3$ and KNbO$_3$. For these reasons, the method of ion implantation is especially well suited for perovscites [91, 92] as well as for crystals of the tungsten-bronze family, in particular SBN [93]. The implantation of light ions like H$^+$ and He$^+$ with energies of some MeV has successfully been used for waveguide formation in a wide range of optical materials, including photore-fractive ferroelectrics and sillenites. Apart from epitaxial techniques like PLD, ion implantation today is the only method that reliably results in low-loss single crystalline waveguides for BaTiO$_3$, KNbO$_3$, or SBN.

Impinging upon the crystal, the implanted ions slow down because of energy loss from interactions with the electrons of the target. At the end of their path, the ions' energy is in the range of some keV. Here, nuclear collision sets in, producing a well-defined damaged barrier layer with reduced refractive index. Light is guided above the barrier layer in the region of electron excitation. A typical magnitude of the refractive index decrease is about 5% of the sub-strate value; deeper barriers up to 10% have been obtained for KNbO$_3$ [13].

The ion-dose dependence of the refractive index decrease generally shows a saturation behavior, whereas the initial growth rate and the saturation level depend on ion energy [12]. Because of the well-defined penetration depth of the ions, nearly step-like refractive index profiles are obtained by ion implantation. Optical tunneling through the barrier, however, can lead to an increase of propagation losses for large mode numbers. Besides this mechanism, the loss

mechanism in ion-implanted waveguides is rather complex. It consists of contributions by material and implantation-induced absorption as well as surface scattering. A detailed overview on optical effects of ion implantation can be found in [94].

To a large extent, the electro-optic and photorefractive properties of the bulk crystal are maintained in the waveguiding layer. Frequently observed is a chemical reduction of the waveguiding layer as a result of the implantation process [95, 96]. Moreover, the electro-optic coefficients may be reduced due to depolarization effects [97, 98]. For a low dose of the implanted ions in the range of some 10^{13} to $10^{15}\,\mathrm{cm}^{-2}$, a slight increase of the extraordinary refractive index has been observed for several ferroelectric crystals [99]. This effect has been used to fabricate nonleaky waveguides [100], where light is confined without the possibility of barrier tunneling. Higher doses of $10^{16}\,\mathrm{cm}^{-2}$ and more have resulted in a decrease of both refractive indices. Furthermore, the implantation through an appropriate mask on the substrate surface has enabled the fabrication of both single and multimode channel waveguides in various materials [99, 101].

10.4.2 Barium Titanate

Photorefractive barium titanate ($BaTiO_3$) crystals are currently used for a wide range of nonlinear optical applications [1, 102, 103]. One of the most interesting features of $BaTiO_3$ is its electro-optic coefficient $r_{51} \approx 1600\,\mathrm{pm/V}$, which is one of the largest values known for any crystal. However, the practical use of $BaTiO_3$ crystals is at least partially limited by the relatively long response time of grating formation. Obviously, a significant decrease in response time can be achieved by using planar $BaTiO_3$ waveguides, i.e., by making use of the high intensities inherent in waveguide geometries. Another drawback of $BaTiO_3$ is a phase transition that occurs around 6 °C that is connected with mechanical stress to the samples and therefore may result in cracking of the crystal. Here $BaTiO_3$ may be replaced by barium-calcium titanate (BCT) crystals, a material with very similar electro-optic and photorefractive properties where this problematic phase transition is missing.

Planar optical waveguides in $BaTiO_3$ were first fabricated by Moretti et al. [91] in 1990 by implantation of 2 MeV He^+ at a dose of $10^{16}\,\mathrm{cm}^{-2}$. Both the ordinary and the extraordinary refractive index were decreased in the region of the implanted barrier [104]. Two-wave mixing in a 1.5 MeV H^+-implanted $BaTiO_3$ waveguide was reported by Youden et al. [105] in 1992. In Fig. 10.5, a decrease of response time of about two orders of magnitude when compared to the response time at same input power in the substrate has been observed. Frequently, the beam coupling direction is reversed to that of the substrate. This can probably be attributed to a change in the dominant charge carrier species from holes to electrons because of electrochemical reduction of impurities by the ion beam. Two-wave mixing even at 854 nm with a maximum gain of $24\,\mathrm{cm}^{-1}$ has been achieved in a Rh-doped $BaTiO_3$ crystal [106]. Both
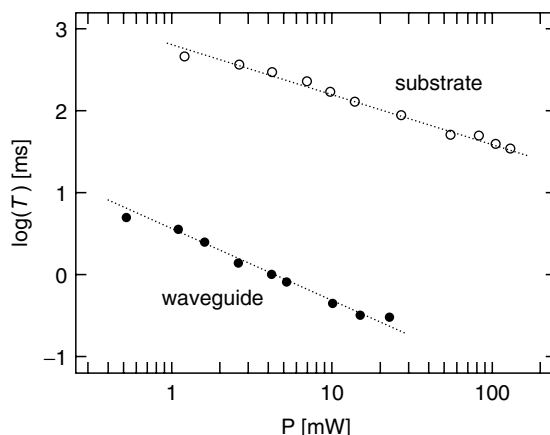
FIGURE. 10.5. Time constant of two-beam coupling measured in a BaTiO$_3$ planar waveguide (•) and in the substrate (○) for the wavelength 488 nm as a function of light power P [105].

self-pumped phase conjugation [107] and mutually pumped phase conjugation [108] in the same sample have been obtained, too.

Epitaxial and very smooth films have been fabricated by PLD combined with *in situ* annealing of the growing film [109, 110]. Planar waveguides with propagation losses of 2 to 3 dB/cm at 633 nm with an electro-optic coefficient of $r_{51} = 86 \, \text{pm/V}$ have been obtained for c-axis films [98]. For a-axis films, an electro-optic coefficient $r_{\text{eff}} = 536 \, \text{pm/V}$ has been found for low applied electric fields. A variety of other deposition techniques has successfully been used for the formation of BaTiO$_3$ thin films on adequate substrates, e.g., by MBE, the sol-gel process, or MOCVD. With MOCVD, channel waveguides have been fabricated using an additional etching in HF solution. These waveguides have shown moderate optical loss of 1 to $2 \, \text{cm}^{-1}$ at $1.55 \, \mu\text{m}$ [111] and effective electro-optic coefficients of about 50 pm/V [112].

10.4.3 Potassium Niobate

Potassium niobate (KNbO$_3$) belongs to the most promising ferroelectric oxides with excellent optical properties [113]. Large nonlinear and electro-optic coefficients in the spectral range of visible and infrared diode lasers and a high photorefractive sensitivity make the crystal a particularly attractive candidate for applications in integrated optics.

Methods of waveguide formation that have been successfully applied to other materials like diffusion or ion exchange have been found to be not applicable to KNbO$_3$, probably because of the densely packed lattice of the perovscite structure. The first permanent waveguides in KNbO$_3$ were realized by implantation of He$^+$ in 1988 by Bremer et al. [102]. Low-loss planar waveguides with damping coefficients of about $1 \, \text{cm}^{-1}$ (wavelength 632.8 nm) can be formed by He$^+$

implantation at low doses of some 10^{14} cm^{-2} [114]. Even lower propagation loss of only 0.2 cm^{-1} has been found for a slightly higher dose of $1.5 \cdot 10^{15}$ cm^{-2} [115]. For H$^+$ implantation, doses of 10^{16} cm^{-2} and higher are used to produce good optical waveguides; here damping coefficients of 1 to 3 cm^{-1} for visible light have been reported [116, 117]. Channel waveguides in KNbO$_3$ with damping coefficients as low as 0.3 cm^{-1} for red light have been realized by Fluck et al. [101] by repeated He$^+$ implantation as well as by ultra-low dose implantation that leads to an increase of the refractive index of the implanted area [100].

Two-wave mixing experiments have been performed to characterize the photorefractive properties of iron-implanted planar waveguides in KNbO$_3$. Both H$^+$ and He$^+$ implantation have been used in nominally pure and iron-doped substrate crystals. In all published work, the beam coupling direction in the implanted waveguides in KNbO$_3$ was reversed to that of the substrate [118], and high logarithmic gain coefficients up to 40 cm^{-1} have been obtained [116]. Smaller beam coupling coefficients of 2.2 cm^{-1} and a response time of only 60 ms have been measured for a wavelength of 1.3 μm in a H$^+$-implanted KNbO$_3$: Fe waveguide [117].

To fabricate thin films of KNbO$_3$, different deposition techniques like LPE, MOCVD, PLD, ion beam, or rf-sputtering have been used to fabricate single-crystal layers of KNbO$_3$ for applications in nonlinear optics. For the last method, a SHG coefficient of 5 pm/V, which is one third of the bulk value, has been reported [119], and higher coefficients of almost the bulk value have been measured in samples prepared by MOCVD [120].

10.4.4 Other Materials

In several other photorefractive perovscite crystals, waveguiding layers have been fabricated. These crystals include potassium-tantalate niobate (KTN), KTa$_{1-x}$Nb$_x$O$_3$, and barium-strontium titanate (BST), Ba$_{1-x}$Sr$_x$Ti$_2$O$_6$. In the KTN crystallographic system, the largest electro-optic coefficients among all photorefractive oxide crystals are found: The value of r_{51} can approach 10^4. Waveguides in this material have been formed by ion-implantation [121]. By PLD thin films of usually polycrystalline BST have been deposited on different substrates like MgO(001) and sapphire, and a large quadratic electro-optic coefficient of 1×10^{15} m^2/V^2 has been measured [122].

10.5 Materials with Tungsten-Bronze Structure

10.5.1 Strontium-Barium Niobate (SBN)

Strontium-barium niobate crystals (Sr$_x$Ba$_{1-x}$Nb$_2$O$_6$, $0.25 \leq x \leq 0.75$, SBN) are characterized by particularly large pyro- and piezoelectric, electro- and thermo-optic coefficients, robustness, and an excellent optical quality. The electro-optic coefficients are about ten (SBN61) to forty times (SBN75) larger

than those in $LiNbO_3$. The most widely investigated composition is the congruently melting one, $x = 0.61$ (SBN61). Another interesting composition is the strontium-enriched $x = 0.75$ (SBN75) with a lowered phase transition temperature. The open tungsten bronze structure allows doping with a variety of rare-earth and transition metal materials to improve the photorefractive sensitivity. SBN permits many applications in optical data storage and processing [123, 124], and a lot of fundamental research has been done demonstrating the excellent photorefractive properties of this material [125, 126]. Since the discovery of the photorefractive soliton in 1992/1993 [127, 128], SBN has become the most widely used material in this outstanding research field.

Planar waveguide formation in SBN by He^+ implantation was first mentioned by Youden et al. [105] in 1992, and later was investigated in more detail in [103]. Low-loss waveguides ($0.35\,cm^{-1}$ at the wavelength 632.8 nm) are obtained for low-dose He^+ implantation or intermediate doses using H^+. The photorefractive properties of SBN61 and SBN75 waveguides formed by H^+ or He^+ implantation are investigated in Refs. [95, 129]. When compared to data for the bulk material at the same intensity, the response time for two-wave mixing in SBN waveguides is decreased by one or two orders of magnitude both for H^+ [95] and low-dose He^+ [129] implantation. In the latter work, with an increasing dose of implanted He^+, a strong degradation of the photorefractive properties was observed. High logarithmic gain coefficients of up to $45\,cm^{-1}$ with time constants of the order of milliseconds have been obtained for extraordinarily polarized blue light, adequate cerium doping, and optimized implantation parameters [129].

Polycrystalline SBN thin films of various compositions have been obtained by LPE, rf-sputtering, MOCVD [120], and the sol-gel process. Epitaxial SBN61 [130] and SBN75 [131] films on MgO substrates with high electrooptic coefficients r_{33} of 380 pm/V and 844 pm/V, respectively, have been fabricated by PLD, but only little is known about the optical properties of such films [132].

Planar and channel waveguide formation in SBN substrate crystals has been also performed using sulphur [133] and zinc [134] indiffusion, but the achieved waveguides exhibit high losses greater than $2.5\,cm^{-1}$. Recently, channel waveguides in SBN have been fabricated by a refractive index increase because of the static strain-optic effect [135] and fast electro-optic modulation in the GHz range has been demonstrated [136].

10.5.2 Other Materials

Apart from SBN, waveguides in other tungsten bronze crystals have recently received considerable attention, too. Well known examples are potassium-sodium strontium-barium niobate $(K_yNa_{1-y})_{2A-2}(Sr_xBa_{1-x})_{2-A}Nb_2O_6$ (KNSBN) and barium-strontium titanate-niobate $Ba_{1-x}Sr_xTi_yNb_{2-y}O_6$ (BSTN). Planar waveguides have been fabricated by ion implantation in KNSBN, and two-wave mixing experiments have been performed [137, 138]. Low-loss, strain-induced waveguides have been also formed in BSTN [139].

10.6 Sillenites

Sillenite crystals of the type $Bi_{12}MO_{20}$ with M = Si (BSO), Ge (BGO), and Ti (BTO) possess a large photoconductivity and holographic sensitivity for visible and near-infrared light, which makes these materials attractive candidates for applications of dynamic holography and optical phase conjugation. For the fabrication of waveguides in sillenites, LPE, i.e., the thermally-controlled over-growth of single-crystal films from the melt on a single-crystalline substrate may be used. When compared to MBE, the uniformity and surface morphology of LPE films are poor, but deposition rates are high. Together with PLD and in part also ion implantation, LPE is the preferred method to form waveguides in the sillenites BGO, BTO, and BSO.

The fabrication of optical waveguides in sillenites has been reported in quite a few papers, however, only little is known about the photorefractive properties of these samples. Waveguiding has been observed in epitaxial BTO films fabricated by LPE on BGO substrates [140], as well as BGO and BSO layers formed by PLD on single-crystalline zirconia and sapphire [141, 142]. For the latter, electrooptic and nonlinear optical properties have been proved [143]. Two-wave mixing in planar BTO waveguides grown on BGO and BSO substrates by LPE has been observed in [144, 145]. To improve the photorefractive properties of these BTO waveguides, the melts have been doped with d-(Cu, Cr, Fe, Co, Ni), p-(Ga) and s-(Ca) elements of the periodic table. The measured electro-optic coefficients as well as the beam coupling gain have been found to be lower than for the bulk material, but high two-beam coupling coefficients up to $8\,cm^{-1}$ have been found for copper doping of BTO layers. An increase of the gain value has been also obtained by applying an external electric AC field along the grating direction [146].

10.7 Applications

Since the first fabrication of optical waveguides in $LiNbO_3$ in 1974, a large number of different optical components based on photorefractive waveguides has been proposed, and devices like spectrometers, optical amplifiers, phase conjugators, reconfigurable optical interconnections, or narrow-bandwidth filters have been experimentally demonstrated. Corresponding to the various applications, quite different requirements of waveguide and photorefractive parameters have to be fulfilled. In the following section, some of the applications of photorefractive waveguides will be presented.

10.7.1 Optical Interconnections

Different types of optical switches and interconnections using photorefractive waveguides have been experimentally investigated. Holographic interconnections in a planar $LiNbO_3$ waveguide have been proposed in [147] and further

developed and experimentally confirmed about ten years later in [148]. In [149] an array of intersecting parallel channel waveguides in $LiNbO_3$, where coupling is obtained via holographic gratings in the overlap regions, has been used. Another method uses an array of reconfigurable photorefractive waveguides for optical interconnections, where either a bulk $LiNbO_3$ crystal is illuminated by an interference fringe pattern [150] or by three dimensional scanning of a focused laser [151, 152]. A recent review of these works can be found in [153]. Very recently reconfigurable optical interconnections have been also realized in the crystal $KNbO_3$. Here optical channel waveguides are formed by illuminating a crystal surface with a focused UV beam using the inter-band photorefractive effect in $KNbO_3$. An even more promising alternative for dynamic interconnections is the use of spatial solitons, which is explained in short in the next subsection.

10.7.2 Spatial Solitons

Since their discovery in 1992/1993, photorefractive spatial solitons have attracted considerable interest [127, 128]. Only low power levels of the order of microwatts are necessary to form these non-diffracting beams. Solitons possess unique properties, for instance in their interaction, which make them attractive for all-optical switches and routers. Chapter 11 of this book extensively treats the interesting properties of photorefractive solitons, so we will here concentrate on special features of photorefractive solitons in waveguides.

In planar waveguides, spatial solitons are formed in a true $(1+1)$-dimensional medium, thus getting rid of the transverse instability that is inherent to soliton formation in bulk crystals. Moreover, for applications in switching and routing, the planar waveguide's geometry is easily compatible with fiber optics. Photorefractive bright spatial solitons have been formed in $Sr_{0.61}Ba_{0.310}Nb_2O_6$ (SBN) waveguides produced by He^+-implantation [154]. Here, photorefractive solitons can be formed over a wide wavelength range, from visible to telecommunication wavelengths up to $1.5\,\mu m$ [97]. The suitability for beam steering and forming as well as for switching and routing by interaction of solitons and applications such as y-junctions has been demonstrated [155, 156]. Dark photovoltaic solitons have been studied in $LiNbO_3$ planar waveguides fabricated by indiffusion of titanium, iron, and copper [157].

10.7.3 Reflection Filters

In the last few years, fiber Bragg gratings (FBG) have achieved considerable interest for applications as optical sensors for the measurement of, e.g., temperature, vibrations, or mechanical stress, for uses as fiber laser resonators, or for dense wavelength division multiplexing (DWDM). All of these devices make use of the narrow spectral bandwidth of the recorded reflection gratings in photosensitive glass fibers. In some of these devices, the peak reflection

wavelength is adjusted by external mechanical stress on the fiber using piezo drivers.

A promising alternative to FBGs in glass are holographically recorded refractive index gratings in channel waveguides in $LiNbO_3$ [158]. Such single mode waveguides for infrared light around $1.55 \mu m$ can be formed by titanium in-diffusion. To increase their holographic sensitivity and light-induced refractive index changes, the samples can additionally be diffusion-doped with either iron or copper. In combination with a thermal fixing technique of the refractive index patterns [21, 159], which makes the gratings insensitive against the erasure with visible light, this allows to design a variety of devices that operate in the infrared wavelength region.

A scheme of the holographic recording geometry is given in Fig. 10.6. Light of the photosensitive blue or green spectral region is used to record a grating for the infrared in a standard two-beam setup using external writing beams. The grating is directed along the c-axis, and for proper choice of the waveguide fabrication parameters the filter works polarization independent. In this way, peak reflectivities exceeding 99.9% and bandwidths of 0.1 nm (FWHM) for a 15 mm-long grating have been obtained. Such gratings are of large interest for application as electrically switchable add-drop-filters in DWDM [158] or for use as mirrors for integrated lasers [21].

10.7.4 Integrated Sagnac-Interferometers

A practical example of integrated optics in $LiNbO_3$ that suffers from photorefractive effects are laser gyros or Sagnac interferometer, respectively, which are used for the precise measurement of small angular velocities with application in car navigation, aviation, or rocket stabilization [160]. In such a device, the light of a coherent polarized light source with frequency ω_0 is split in two parts, then passes a polarization maintaining fiber coil in two opposite directions, and finally the two counterpropagating waves interfere on a photodiode.
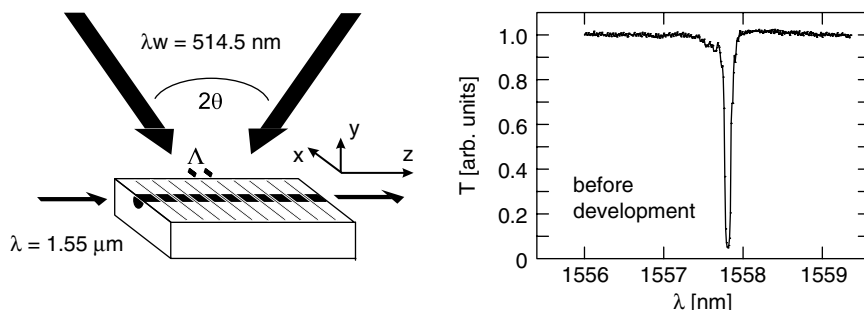

FIGURE. 10.6. Holographically recorded reflection filters in $LiNbO_3$: Ti: Cu channel waveguides. a) Geometry for recording and read-out of the grating, and b) typical transmission spectrum $T(\lambda)$ of a 15 mm-long filter.
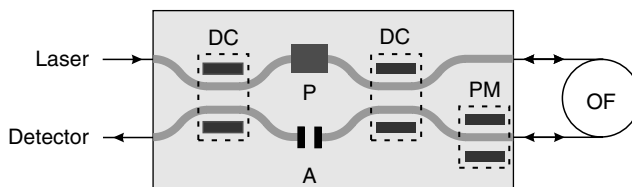
310   Detlef Kip and Monika Wesner

FIGURE. 10.7. Example of an integrated Sagnac interferometer for rotation sensing. DC, electrically adjustable directional couplers; P, polarizer; A, light absorbers; PM, phase modulator; OF, optical fiber coil.

When the fiber coil of diameter D and length L rotates with an angular velocity Ω, a phase difference

$$\Delta_\gamma = \frac{LD\omega_0\Omega}{c^2} \qquad (10.4)$$

is measured in the output interference signal, where c is the speed of light in vacuum. In a standard configuration, a phase modulator in one arm of the interferometer leads to an additional difference phase modulation of the output signal, which can be used for a closed-loop operation of the Sagnac interferometer.

Because of the high requirements on stability and exact reciprocity of the device and the need for phase modulation of the optical signals, a realization of a compact, integrated optical Sagnac interferometer in $LiNbO_3$ is favorable. Such a component where all optical components are integrated on a single chip is shown in Fig. 10.7. Today, these devices are in use, e.g., in civil and military aviation. However, although much work has been spent on the optimization of design and production techniques, the fabrication yield is still heavily limited and may be as low as about ten percent in some cases, which can be at least in part attributed to undesired photorefractive effects in the $LiNbO_3$ chip [161].

10.8 Conclusions and Outlook

In this chapter, recent results on formation and investigation of photorefractive waveguides have been summarized, and some interesting applications of these samples have been outlined. Further improvement and simplification of the necessary fabrication technologies, e.g., by low-cost thin film deposition, as well as tailored photorefractive properties and geometries of the waveguides, will stimulate future developments in this active research area.

References

1. P. Günter, J.-P. Huignard (Eds.): *Photorefractive Materials and Their Applications I+II*, Topics Appl. Phys., Vol. 61 and 62, Springer-Verlag, Berlin (1998).

2. M.P. Petrov, S.I. Stepanov, A. Khomenko (Eds.): *Photorefractive Crystals in Coherent Optical Systems*, Springer-Verlag, Berlin (1991).

3. An older but excellent review of this topic can be found in V.E. Wood, P.J. Cressman, R.L. Holman, C.M. Verber: in *Photorefractive Materials and Their Applications II*, P. Günter, J.-P. Huignard (Eds.), Topics Appl. Phys., Vol. 62, Springer-Verlag, Berlin (1988).

4. D. Kip: Appl. Phys. B **67**, 131 (1988).

5. A.M. Prokhorov, Y.S. Kuzminov: *Ferroelectric Thin-Film Waveguides in Integrated Optics*, Cambridge International Science, Cambridge (1996).

6. V. Gericke, P. Hertel, E. Krätzig, J.P. Nisius, R. Sommerfeld: Appl. Phys. B **44**, 155 (1987).

7. D. Fluck, J.A. Weiss, S. Brülisauer, P. Günter: Opt. Lett. **19**, 2080 (1994).

8. L. Wan, Y. Yuan, G. Assanto: Opt. Commun. **73**, 4310 (1989).

9. L. Wan, Y. Yuan, G. Assanto: Opt. Commun. **74**, 361 (1990).

10. A. Yamada, H. Tamada, M. Saitoh: J. Appl. Phys. **76**, 1776 (1994).

11. P.K. Tien, R. Ulrich: J. Opt. Soc. Am. **60**, 1325 (1970).

12. L. Zhang, P.J. Chandler, P.D. Townsend: Nucl. Instr. and Meth. B **59/60**, 1147 (1991).

13. D. Fluck, D.H. Jundt, P. Günter, M. Fleuster, C. Buchal: J. Appl. Phys. **74**, 6023 (1993).

14. P. Hertel, H.P. Menzler: Appl. Phys. B **44**, 75 (1987).

15. S. Herminghaus, B.A. Smith, J.D. Swalen: J. Opt. Soc. Am. B **8**, 2311 (1991).

16. F. Rickermann, D. Kip, B. Gather, E. Krätzig: phys. stat. sol. (a) **150**, 763 (1995).

17. I. Savatinova, S. Tochev, R. Todorov, M.N. Armenise, V.M.N. Passaro, C.C. Ziling: J. Lightwave Technol. **14**, 403 (1996).

18. T. Yuhara, K. Tada, Y.-S. Li: J. Appl. Phys. **71**, 3966 (1992).

19. P.G. Suchoski, T.K. Findakly, F.J. Leonberger: Opt. Lett. **13**, 1050 (1988).

20. T. Suzuki, O. Eknoyan, H.F. Taylor: J. Lightwave Technol. **11**, 285 (1993).

21. B.K. Das, R. Ricken, W. Sohler: Appl. Phys. Lett. **82**, 1515 (2003).

22. A. Yamada, H. Tamada, M. Saitoh: J. Cryst. Growth **132**, 48 (1993).

23. F. Gitmans, Z. Sitar, P. Günter: Vacuum **46**, 939 (1995).

24. Y. Kondo, T. Kouyama, K. Ohno, M. Tsuji, M. Nakamura, Y. Fujii: Jpn. J. Appl. Phys. **33**, L338 (1994).

25. W.S. Hu, Z.G. Liu, Y.-Q. Lu, S.N. Zhu, D. Feng: Opt. Lett. **21**, 946 (1996).

26. S. Fries, P. Hertel, H.P. Menzler: phys. stat. sol. (a) **108**, 449 (1988).

27. V.V. Atuchin, K.K. Ziling, D.P. Shipilova: Sov. J. Quant. Electron. **14**, 671 (1984).

28. R.J. Holmes, D.M. Smyth: J. Appl. Phys. **55**, 3531 (1984).

29. M. De Sario, M.N. Armenise, C. Canali, A. Carnera, P. Mazzoldi, G. Celotti: J. Appl. Phys. **57**, 1482 (1985).

30. R.V. Schmidt, I.P. Kaminow: Appl. Phys. Lett. **25**, 458 (1974).

31. W.M. Young, R.S. Feigelson, M.M. Fejer, M.F.J. Digonnet, H.J. Shaw: Opt. Lett. **16**, 995 (1991).

32. Y. Shigematsu, M. Fujimura, T. Suhara: Jap. J. Appl. Phys. **41**, 4825 (2002).

33. J.M. Hammer, W. Phillips: Appl. Phys. Lett. **24**, 545 (1974).

34. A.D. Novikov, S.G. Odoulov, V.M. Shandarov, S.M. Shandarov: Sov. Phys. Tech. Phys. **33**, 969 (1988).

35. D. Kip, B. Gather, H. Bendig, E. Krätzig: phys. stat. sol. (a) **139**, 241 (1993).

36. J.L. Jackel, C.E. Rice, J.J. Veselka: Ferroelectrics **50**, 165 (1983).

312   Detlef Kip and Monika Wesner

37. J.M. Cabrera, J. Olivares, M. Carrascosa, J. Rams, R. Müller, E. Dieguez: Adv. Phys. **45**, 349 (1996).
38. V.A. Ganshin, Y.N. Korkishko, T.V. Morozova, V.V. Saraikin: phys. stat. sol. (a) **114**, 457 (1989).
39. V.V. Atuchin, T.I. Zakharyash: Sov. Phys. Tech. Phys. **29**, 584 (1984).
40. W.Y. Hsu, C.S. Willand, V. Gopalan, M. Gupta: Appl. Phys. Lett. **61**, 2263 (1992).
41. K. Tada, T. Murai, T. Nakabayashi, T. Iwashima, T. Ishikawa: Jpn. J. Appl. Phys. **26**, 503 (1987).
42. K. Yamamoto, T. Taniuchi: J. Appl. Phys. **70**, 6663 (1991).
43. R.A. Becker: Appl. Phys. Lett. **43**, 131 (1986).
44. Y.N. Korkishko, V.A. Fedorov: J. Appl. Phys. **82**, 99 (1997).
45. M. Minakata, K. Kumagi, S. Kawakami: Appl. Phys. Lett. **49**, 992 (1986).
46. N. Goto, G.L. Yip: Appl. Opt. **28**, 60 (1989).
47. A. Mendez, G. De la Paliza, A. Garcia-Cabanes, J.M. Cabrera: Appl. Phys. B **73**, 485 (2001).
48. H. Ahlfeldt, F. Laurell, G. Arvidsson: Electron. Lett. **29**, 819 (1993).
49. Y.N. Korkishko, V.A. Federov, A.N. Alkaev, F. Laurell: Appl. Phys. B **73**, 519 (2001).
50. J. Rams, J.M. Cabrera: J. Opt. Soc. Am. B **16**, 401 (1999).
51. R. Osellame, R. Ramponi, M. Marangoni, V. Russo: Electron. Lett. **36**, 431 (2000).
52. D.H. Tsou, M.H. Chou, P. Santhanaraghavan, Y.H. Chen, Y.C. Huang: Mat. Chem. Phys. **78**, 474 (2002).
53. S.M. Kostritskii, D. Kip, E. Krätzig: Appl. Phys. B **65**, 517 (1997).
54. R. Göring, Z. Yuan-Ling, S. Steinberg: Appl. Phys. A **55**, 97 (1992).
55. K. Buse: Appl. Phys. B **64**, 273 (1997).
56. F. Jermann, J. Otten: J. Opt. Soc. Am. B **10**, 2085 (1993).
57. Y. Kondo, S. Miyaguchi, A. Onoe, Y. Fujii: Appl. Opt. **33**, 3348 (1994).
58. J. Jackel, A.M. Glass, G.E. Petersen, C.E. Rice, D.H. Olsen, J.J. Veleska: J. Appl. Phys. **55**, 269 (1984).
59. J. Olivares, E. Dieguez, F.J. Lopez, J.M. Cabrera: Appl. Phys. Lett. **61**, 624 (1992).
60. J.J. Amodei, D.L. Staebler: Appl. Phys. Lett. **18**, 540 (1971).
61. A. Mendez, A. Garcia-Cabanes, M. Carrascosa, J.M. Cabrera: Opt. Mat. **18**, 111 (2001).
62. A. Mendez, A. Garcia-Cabanes, M. Carrascosa, J.M. Cabrera: J. Opt. Soc. Am. B **17**, 1412 (2000).
63. S. Tan, T. Gilbert, C.-Y. Hung, T.E. Schlesinger, M. Migliuolo: J. Appl. Phys. **79**, 3548 (1996).
64. K. Nashimoto, M.J. Cima: Mater. Lett. **10**, 348 (1991).
65. M. Aguilar, M. Carrascosa, F. Agullo-Lopez, L.F. Magana: J. Appl. Phys. **78**, 4840 (1995).
66. I.I. Itkin, S.M. Shandarov: Sov. Phys. Tech. Phys. **35**, 1317 (1990).
67. P.G. Kazansky: IEEE J. Quant. Electron. **QE-25**, 736 (1989).
68. D. Kip, R. Fink, T. Bartholomäus, E. Krätzig: Opt. Commun. **95**, 33 (1993).
69. D. Kip, F. Rickermann, E. Krätzig: Opt. Lett. **20**, 1139 (1995).
70. A.D. Novikov, S.G. Odoulov, V.M. Shandarov, E.S. Shandarov, S.M. Shandarov: J. Opt. Soc. Am. B **8**, 1298 (1991).
71. V.L. Popov, E.S. Shandarov, S.M. Shandarov: J. Opt. Soc. Am. B **9**, 1661 (1992).
72. D. Kip, E. Krätzig: Opt. Lett. **17**, 1563 (1992).

73. E.M. Zolotov, P.G. Kazansky, V.A. Chernykh: Sov. Tech. Phys. Lett. **7**, 397 (1981).
74. I.I. Itkin, S.M. Shandarov: Sov. Tech. Phys. Lett. **16**, 357 (1990).
75. Y. Solomonov, S.M. Shandarov, V.M. Shandarov: Ferroelectrics **201**, 195 (1997).
76. V.I. Belinicher, B.I. Sturman: Sov. Phys: Uspheki **23**, 199 (1980).
77. S.G. Odoulov: Sov. Phys. JETP Lett. **35**, 10 (1982).
78. T. Fujiwara, X. Cao, R. Srivastava, R.V. Ramaswamy: Appl. Phys. Lett. **61**, 743 (1992).
79. T. Fujiwara, R. Srivastava, X. Cao, R.V. Ramaswamy: Opt. Lett. **18**, 346 (1993).
80. S. Steinberg, R. Göring, T. Hennig, A. Rasch: Opt. Lett. **20**, 683 (1995).
81. M. Rottschalk, T. Bachmann, S. Steinberg, J.-P. Ruske: Opt. Commun. **106**, 187 (1994).
82. E.E. Robertson, R.W. Eason, Y. Yokoo, P.J. Chandler: Appl. Phys. Lett. **70**, 2094 (1997).
83. D. Eger, M.A. Arbore, M.M. Fejer, M.L. Bortz: J. Appl. Phys. **82**, 1998 (1997).
84. P.J. Matthews, A.R. Mickelson: J. Appl. Phys. **71**, 5310 (1992).
85. D.B. Maring, R.F. Tavlykaev, R.V. Ramaswamy, S.M. Kostritskii: J. Opt. Soc. Am. B **19**, 1575 (2002).
86. O. Eknoyan, H.F. Taylor, W. Matous, T. Ottinger, R.R. Neurgaonkar: Appl. Phys. Lett. **71**, 3051 (1997).
87. Y. Kondo, Y. Fujii: Jpn. J. Appl. Phys. **34**, L365 (1995).
88. D. Kip, T. Bartholomäus, P.M. Garcia, E. Krätzig: J. Opt. Soc. Am. B **11**, 1737 (1994).
89. S. Kostritskii, D. Kip: phys. stat. sol. (a) **169**, 171 (1998).
90. H. Xie, W.-H. Hsu, R. Raj: J. Appl. Phys. **77**, 3420 (1995).
91. P. Moretti, P. Thevenard, G. Godefroy, R. Sommerfeld, P. Hertel, E. Krätzig: phys. stat. sol. (a) **117**, K85 (1990).
92. T. Bremer, W. Heiland, B. Hellermann, P. Hertel, E. Krätzig, D. Kollewe: Ferroelectrics Lett. **9**, 11 (1988).
93. D. Kip, S. Aulkemeyer, P. Moretti: Opt. Lett. **20**, 1256 (1995).
94. P. Townsend, P.J. Chandler, L. Zhang: *Optical Effects of Ion Implantation*, Cambridge University, Cambridge, UK (1994).
95. E.E. Robertson, R.W. Eason, M. Kaczmarek, P.J. Chandler, X. Huang: Opt. Lett. **21**, 641 (1996).
96. S. Brülisauer, D. Fluck, P. Günter, L. Beckers, C. Buchal: Opt. Commun. **153**, 375 (1998).
97. M. Wesner, C. Herden, D. Kip, E. Krätzig, P. Moretti: Opt. Commun. **188**, 69 (2001).
98. A. Petraru, J. Schubert, M. Schmid, Ch. Buchal: Appl. Phys. Lett. **81**, 1375 (2002).
99. P.D. Townsend: Nucl. Instr. and Meth. B **46**, 18 (1990).
100. F.P. Strohkendl, D. Fluck, P. Günter, R. Irmscher, C. Buchal: Appl. Phys. Lett. **59**, 3354 (1991).
101. D. Fluck, P. Günter, M. Fleuster, C. Buchal: J. Appl. Phys. **72**, 1671 (1992).
102. T. Tschudi, A. Herden, J. Goltz, H. Klumb, F. Laeri, J. Albers: IEEE J. Quant. Electron. **QE-22**, 1493 (1986).
103. Z. Zhang, Y. Zhang, C. Yang, J. Kang, S. Zheng, Y. Zhu, Y. Chen, X. Wu, P. Fu: J. Opt. Soc. Am. B **11**, 1991 (1994).
104. P. Moretti, P. Thevenard, R. Sommerfeld, G. Godefroy: Nucl. Instr. and Meth. B **59/60**, 1228 (1991).

314   Detlef Kip and Monika Wesner

105. K.E. Youden, S.W. James, R.W. Eason, P.J. Chandler, L. Zhang, P.D. Townsend: Opt. Lett. **17**, 1509 (1992).
106. P. Mathey, A. Dazzi, P. Jullien, D. Rytz, P. Moretti: J. Opt. Soc. Am. B **18**, 344 (2001).
107. S.W. James, K.E. Youden, P.M. Jeffrey, R.W. Eason, P.J. Chandler, L. Zhang, P.D. Townsend: Opt. Lett. **18**, 1138 (1993).
108. S.W. James, K.E. Youden, P.M. Jeffrey, R.W. Eason, P.J. Chandler, L. Zhang, P.D. Townsend: Appl. Opt. **32**, 5299 (1993).
109. A. Ito, A. Machida, M. Obara: Jpn. J. Appl. Phys. **36**, L805 (1997).
110. L. Beckers, J. Schubert, W. Zander, J. Ziesmann, A. Eckau, P. Leinenbach, C. Buchal: J. Appl. Phys. **83**, 3305 (1998).
111. D.M. Gill, B.A. Block, C.W. Conrad, B.W. Wessels, S.T. Ho: Appl. Phys. Lett. **69**, 2968 (1996).
112. D.M. Gill, C.W. Conrad, G. Ford, B.W. Wessels, S.T. Ho: Appl. Phys. Lett. **71**, 1783 (1997).
113. P. Günter: Phys. Rep. **93**, 199 (1982).
114. F.P. Strohkendl, P. Günter, C. Buchal, R. Irmscher: J. Appl. Phys. **69**, 84 (1991).
115. T. Pliska, D. Fluck, P. Günter, L. Beckers, C. Buchal: J. Opt. Soc. Am. B **15**, 628 (1998).
116. S. Brülisauer, D. Fluck, P. Günter: Electron. Lett. **31**, 312 (1995).
117. S. Brülisauer, D. Fluck, P. Günter, L. Beckers, C. Buchal: J. Opt. Soc. Am. B **13**, 2544 (1996).
118. M. Zha, D. Fluck, P. Günter, M. Fleuster, C. Buchal: Opt. Lett. **18**, 577 (1993).
119. S. Schwyn, H.W. Lehmann, P. Günter: Appl. Phys. Lett. **61**, 373 (1992).
120. M.J. Nystrom, B.W. Wessels, W.P. Lin, G.K. Wong, D.A. Neumayer, T.J. Marks: Appl. Phys. Lett. **66**, 1726 (1995).
121. D. Fluck, R. Gutmann, P. Günter, R. Irmscher: J. Appl. Phys. **70**, 5147 (1991).
122. D.Y. Kim, S.E. Moon, E.K. Kim, S.J. Lee, J.J. Choi, H.E. Kim, S.I. Kwun: J. Korean Phys. Soc. **42**, S1347 (2003).
123. M.D. Ewbank, R.R. Neurgaonkar, W.K.Cory, J. Feinberg: J. Appl. Phys. **62**, 374 (1987).
124. J. Ma, T. Chang, J. Hong, R.R. Neurgaonkar, G. Barbastathis, D. Psaltis: Opt. Lett. **22**, 1116 (1997).
125. G.L. Wood, W.W. Clark III, M.J. Miller, E.J. Sharp, G.J. Salamo, R.R. Neurgaonkar: IEEE J. Quant. Electron. **QE-23**, 2126 (1987).
126. R.A. Vazquez, M.D. Ewbank, R.R. Neurgaonkar: Opt. Commun. **80**, 253 (1991).
127. M. Segev, B. Crosignani, A. Yariv, B. Fischer: Phys. Rev. Lett. **68**, 923 (1992).
128. G. Duree, J.L. Schultz, G. Salamo, M. Segev, A. Yariv, B. Crosignani, P. DiPorto, E. Sharp, R.R. Neurgaonkar: Phys. Rev. Lett. **71**, 533 (1993).
129. D. Kip, B. Kemper, I. Nee, R. Pankrath, P. Moretti: Appl. Phys. B **65**, 511 (1997).
130. Y.Y. Zhu, R.F. Xiao, G.K.L. Wong: J. Appl. Phys. **82**, 4908 (1997).
131. P. Tayebati, D. Trivedi, M. Tabat: Appl. Phys. Lett. **69**, 1023 (1996).
132. X.L. Guo, Z.G. Liu, S.N. Zhu, T. Yu, S.B. Xiong, W.S. Hu: J. Cryst. Growth **165**, 187 (1996).
133. O. Eknoyan, C.H. Bulmer, H.F. Taylor, W.K. Burns, A.S. Greenblatt, L.A. Beech, R.R. Neurgaonkar: Appl. Phys. Lett. **48**, 13 (1986).
134. O. Eknoyan, V.P. Svenson, J.D. Quinn, R.R. Neurgaonkar: Appl. Phys. Lett. **59**, 28 (1991).

135. J.M. Marx, Z. Tang, O. Eknoyan, H.F. Taylor, R.R. Neurgaonkar: Appl. Phys. Lett. **66**, 274 (1995).

136. J.M. Marx, O. Eknoyan, H.F. Taylor, R.R. Neurgaonkar: IEEE Phot. Technol. Lett. **8**, 1024 (1996).

137. F. Lu, M. Q. Meng, K. M. Wang, W. Li, L. Z. Chai, Y. R. Wang, H. C. Chen, D. Y. Shen: Opt. Commun. **140**, 204 (1997).

138. F. Lu, M.Y. Meng, K.M. Wang, X.D. Liu, H.C. Chen, D.Y. Shen: Opt. Lett. **22**, 163 (1997).

139. J.M. Marx, O. Eknoyan, H.F. Taylor, Z. Tang, R.R. Neurgaonkar: Appl. Phys. Lett. **67**, 1381 (1995).

140. E.I. Leonov, S.E. Khabarov, M.S. Vershinin, V.A. Gusev, V.M. Orlov, L.G. Khokha: Sov. Phys. Tech. Phys. **30**, 1307 (1985).

141. K.E. Youden, R.W. Eason, M.C. Gower, N.A. Vainos: Appl. Phys. Lett. **59**, 1929 (1991).

142. T. Okada, F. Yahiro, H. Uetsuhara, Y. Nakata, M. Maeda, S. Higuchi, K. Ueda: Appl. Phys. A **69**, 723 (1999).

143. V. Chevrier, A. Inam, S. Etemad, D. Harris, J.C. Launay: Technical Digest of the Topical Meeting on ''Photorefractive Materials, Effects, and Devices 1993,'' (PRM '93), Kiev, Ukraine, 220 (1993).

144. Y.F. Kargin, I.V. Tsiar, Y.R. Salikaev, S.M. Shandarov: Tech. Phys. Lett. **20**, 1997 (1994).

145. M.N. Frolova, M.V. Borodin, S.M. Shandarov, V.M. Shandarov, Y.F. Kargin, A. Egorysheva, and D. Kip: Europhysics Conference Abstracts Vol. 27E, CF3-6-TUE (2003).

146. Y. Salikaev, S.M. Shandarov, Y. Kargin: Proc. SPIE **2795**, 203 (1996).

147. T. Jannson: J. Opt. Soc. Am. **71**, 342 (1981).

148. D.J. Brady, D. Psaltis: Appl. Opt. **30**, 2324 (1991).

149. L.B. Aronson, L. Hesselink: Opt. Lett. **15**, 30 (1990).

150. O. Matoba, K. Itoh, Y. Ichioka: Opt. Lett. **21**, 122 (1996).

151. K. Itoh, O. Matoba, Y. Ichioka: Opt. Lett. **19**, 652 (1994).

152. O. Matoba, K. Itoh, Y. Ichioka: Opt. Eng. **35**, 2175 (1996).

153. O. Matoba, K. Itoh, K. Kuroda: Proc. IEEE **87**, 2030 (1999).

154. D. Kip, M. Wesner, V.M. Shandarov, P. Moretti: Opt. Lett. **23**, 921 (1998).

155. D. Kip, M. Wesner, C. Herden, V. Shandarov: Appl. Phys. B **68**, 971 (1999).

156. D. Kip, C. Herden, M. Wesner: Ferroelectrics **274**, 135 (2002).

157. V. Shandarov, D. Kip, M. Wesner, J. Hukriede: J. Optics A **2**, 500 (2000).

158. J. Hukriede, D. Runde, D. Kip: J. Phys. D: Appl. Phys. **36**, R1 (2003).

159. J. Hukriede, I. Nee, D. Kip, E. Krätzig: Opt. Lett. **23**, 1405 (1998).

160. K.T.V. Grattan, B.T. Meggit: *Optical Fiber Sensor Technology. Volume 2: Devices and Technology*, Chapman & Hall, London (1998).

161. I.A. Andronova, G.B. Malykin: Phys. Uspekhi **45**, 793 (2002).